Vacuum 146 (2017) 52–62

Contents lists available at ScienceDirect

Vacuum

journal homepage: www.elsevier.com/locate/vacuum

Examination of a 5 A-class cathode with a LaB_6 flat disk emitter in the 2 A–20 A current range

Romain Joussot*, Lou Grimaud, Stéphane Mazouffre

CNRS, ICARE, UPR3021, 1C Av. de la Recherche Scientifique, CS 50060, 45071 Orléans Cedex 2, France

ARTICLE INFO

Article history:
Received 4 May 2017
Received in revised form
11 August 2017
Accepted 11 September 2017
Available online 15 September 2017

Keywords:
Cathodes
Discharge oscillations
Plasma discharge
Thermionic emission
Hall thruster
Electric propulsion

ABSTRACT

Cathodes are electron sources used for gas ionization and ion beam neutralization in Hall thrusters. A laboratory model of a 5 A-class cathode has been experimentally studied in the so-called diode configuration with a flat metal anode. The cathode design is based on the direct heating of a flat disk lanthanum hexaboride (LaB_6) insert to emit electrons. The paper presents the characterization of the LaB_6 cathode operated at xenon mass flow rates between 0.2 and 0.6 mg.s^{-1} with discharge currents ranging from 2 A to 19 A. Electrical parameters and temperature of several parts, including the LaB_6 insert, were collected and analyzed in order to investigate the possibility of operating the cathode in an extended range of discharge current with respect to its nominal condition (5 A at 0.4 mg.s^{-1}). Particular attention was paid to the identification of the discharge mode (spot versus plume) through spectral analysis of discharge current waveforms. Temperature measurements performed with thermocouples reveal that the LaB_6 insert is moderately heated during the cathode operation (about 1600 °C at 19 A), except for the lowest mass flow rate.

1. Introduction

Within the electric space propulsion field, a cathode is a source of electrons. Along with the magnetizing coils, it is a critical component of a Hall Thruster (HT) assembly [1]. The cathode (the term “hollow cathode” is also used in the literature) has two roles during thruster operation. Firstly, it provides electrons towards the anode to counterbalance losses and maintain the plasma discharge. Secondly, it furnishes electrons for ion beam neutralization downstream the thruster exhaust. The electron stream in the plume typically amounts for 80% of the total cathode current [2].

Over the past decades, intensive R&D efforts have been undertaken to produce reliable, high-efficiency cathodes with a life span that is fully compatible with the HT lifetime. In particular, lanthanum hexaboride (LaB_6) is considered as a reliable electron-emitting material for HT cathodes. More than 300 HTs (mostly Russian) have been operated, or are currently operated, in space with LaB_6 cathodes over the last 45 years [3]. The first HT cathode with a LaB_6 insert was proposed in 1963 in Russia [4] and was first operated in space [5] in 1972 coupled with a SPT-60, aboard of a Meteor-1 satellite. Lanthanum hexaboride is currently considered as an insert material due to its significantly higher poisoning resistance [6] than porous tungsten emitters impregnated with a barium calcium aluminate mixture (BaO-W). A LaB_6 cathode therefore allows for simplified handling and startup procedures [7]. This material also shows longer simulated lifetimes than dispenser cathode emitters [7]. Cathodes using a LaB_6 emitter are therefore perfectly suited for high power HTs. However, the LaB_6 insert must be operated at higher temperatures than a BaO-W insert, requiring a high temperature heater which may lead to greater risk of failures [8]. This point is currently under consideration by several research teams [8–10] developing high power HTs.

Current trends regarding the Hall thruster technology indicate a clear interest for high-power electric propulsion devices able to operate at an input power level between 20 kW and 100 kW [11]. In addition to NSSK and orbit transfer maneuvers of geosynchronous communication satellites, Hall thrusters are foreseen as high potential and reliable candidates for missions such as celestial body exploration, trips to far-off planets as well as space cargo and space tug propulsion [2,11]. In this context, the French space agency (CNES) presently supports a research program that aims at developing, building and investigating a high-power cathode able to deliver up to 100 A of electron current, exceeding by far what is available in France at the present time.

* Corresponding author.
E-mail address: romain.joussot@cnrs-orleans.fr (R. Joussot).

http://dx.doi.org/10.1016/j.vacuum.2017.09.021
0042-207X/

This contribution presents results obtained during the first phase of the high-power cathode development project. This phase consists in collecting and analyzing several physical quantities during operation of a 5 A-class cathode. An existing laboratory model of a heated cathode with a LaB_6 emitter was studied in a diode configuration, *i.e.* without HT. The originality of this work is that the cathode design is based on a LaB_6 flat disk emitter. During the last two decades, most of the published works studied HT cathodes using a cylindrical design for the emitting insert (the term "hollow cathode" is often used for such a design). Even though one of first cathode designs that was used with closed drift thrusters in the early 1970–1980s is based on a flat disk shape for the electron emitter [12], such a shape is rarely studied in the literature. The majority of published works with a flat disk shape for the electron emitter is dedicated to cathodes coupled with Hall thrusters [13-17]. To the best of the authors' knowledge only the works published by the group of L.B. King (Michigan Technological University, U.S.A.) were dedicated to study a cathode design based on a flat disk emitter in a diode configuration [18–20]. These works of King's group were mainly focused on bismuth-fed cathode and a few experimental *I-V* characteristics were published, for a different cathode configuration and at different operating conditions to what is reported in the present study. Even though a flat disk emitter requires a continuous heating to maintain the proper temperature for the LaB_6 insert to produce sufficient electrons [21], this shape ensures an homogeneous utilization of the emitter surface in spot mode [22,23]. This is an advantageous in comparison with a cylindrical insert for which, in some cases, only a fraction of the overall axial length of the cylindrical insert is used to emit electrons [24]. In addition, the plasma density distribution in the vicinity of a flat disk emitter is expected to be rather uniform over a large part of the insert surface, inducing a uniform wear of the insert.

This work reports measurements of electrical parameters and temperatures of several cathode parts, including the LaB_6 emitter, during heating of the cathode (*i.e.*, the pre-ignition phase) and normal operation of the cathode (*i.e.*, with the plasma discharge). Our purpose is to study experimentally this cathode design in a diode configuration in order: 1- to help address the lack of knowledge on a cathode design not often studied in the literature; 2- to check if this cathode design can be operated in spot mode at a discharge current up to 20 A; 3- to provide real test cases for comparison with the numerical simulations performed by our colleagues from LAPLACE in Toulouse (France) with their home-designed cathode code [25]. With the aim of testing HT of different power classes, it is important to investigate whether this 5 A-class cathode can be operated in spot mode up to a discharge current of 20 A. It is well known that HT cathodes run in diode configuration exhibit two main discharge modes [26,27]: the spot mode and the plume mode, the latter being detrimental to the cathode lifetime [28] (wear of the cathode body).

2. Experimental setup

2.1. The NExET test bench

Experiments were performed in the NExET (New Experiments on Electric Thrusters) vacuum vessel (Fig. 1). This test bench was commissioned at the ICARE laboratory in November 2008 and is used in conjunction with the PIVOINE-2g chamber [21] to carry out experiments in the field of electric propulsion. The NExET test-bench is a stainless steel chamber, 1.8 m in length and 0.8 m in diameter. It is equipped with a pump stack composed of a large dry pump, a 350 $L.s^{-1}$ turbomolecular pump to evacuate light gases down to 1×10^{-6}mbar-N_2, and a cryogenic pump with a typical surface temperature of 25–35 K (with a pumping speed of

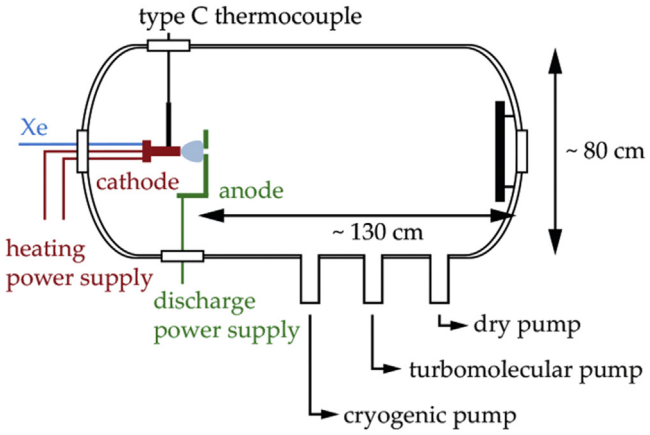

Fig. 1. Schematic of the NExET vacuum vessel with the cathode installed inside.

8000 $L.s^{-1}$) to absorb gases such as Xe and Kr. A large water-cooled screen covered with graphite tiles is mounted at the back of the chamber. It absorbs part of the ion beam energy therefore reducing the thermal load onto the cryogenic surface. A background pressure of 2×10^5 mbar-Xe is achieved inside the chamber with 1 $mg.s^{-1}$ xenon gas flow rate and 250 W input power. The heavy particle momentum exchange mean free path is, in this pressure condition, of the order of the chamber length, which warrants a negligible impact of the residual gas. The chamber is equipped with several observation windows, portholes and diagnostic ports. The interior of the facility is easy to access thanks to a large door located on the front side.

2.2. Cathode configuration

The cathode used in this study is based on a laboratory cathode used usually with the SPT-100-ML [29] (1.5 kW HT derived from the Russian SPT-100 [4]) in the PIVOINE-2g chamber. Since 1996, the usual cathode design used in our vacuum chambers is based on the heating of a flat disk LaB_6 insert (Fig. 2) to emit electrons by thermionic emission. The LaB_6 pellet is enclosed within a cathode body. The orifice diameter of this external body was set to 4.0 mm [14,21]. Even though this orifice diameter seems oversized, it allows a discharge current up to 6 A to be sustained at the nominal mass flow rate of the cathode (0.4 $mg.s^{-1}$ of Xe) [14]. Many studies on HT have been conducted with such a cathode as illustrated by the published works of several research teams [14–17,19].

The cathode architecture is rather simple: the electron emitter is a sintered (*i.e.*, polycrystalline) LaB_6 pellet pressed against a molybdenum pellet holder with a 6 mm-diameter orifice for electron emission. The nominal electron emission surface of the LaB_6 pellet is then 28.27 mm^2. This surface, namely the reference surface S_{ref}

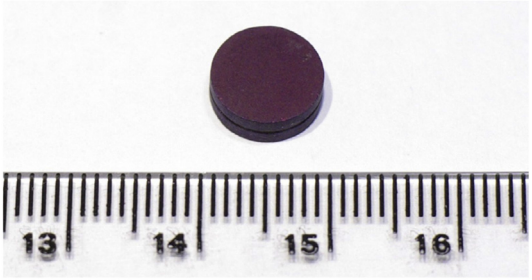

Fig. 2. Picture of the LaB_6 pellet used as electron emitter in the cathode.

($= \pi r_{ref}^2$, with $r_{ref} = 3$ mm), corresponds to the geometrical area of the hole drilled into the pellet holder. The actual emission surface is obviously greater than S_{ref} due to the surface roughness of the LaB_6 pellet. The insert was manufactured by Sindlhauser Materials GmbH and a roughness analysis of the LaB_6 pellet was performed by the manufacturer. The LaB_6 pellet used in this study had a low roughness ($R_a < 0.8$ μm), inducing a small difference between the actual diameter and the reference diameter d_{ref} ($\approx 4\%$). The total uncertainty (see Sect. 2.4) of the reference surface is about 9% in considering a reading error of 100 μm for the reference diameter d_{ref} and the uncertainty due to the surface roughness. A tungsten heater coil is placed behind the pellet in order to raise the emitter to its operating temperature by Joule heating. A dedicated electrical circuit is used to heat the LaB_6 insert (Fig. 3*a*). The heat power is set by the user and ranges from 0 W to 300 W, typically. The LaB_6 insert, the pellet holder, and the heating filament are loosely wrapped in an insulation molybdenum screen in order to minimize radiative losses during emitter heating. These three elements form the internal body of the cathode. As the cathode lifetime required for these experiments is below 200 hr, typically, no barrier layer was set between the LaB_6 insert and the refractory metal parts to prevent boron out-diffusion from the insert [6]. It was assumed that, as long as boron atoms were present in the LaB_6 pellet, only the evaporation rate of the insert was modified, the thermionic emission properties remaining constant during the experiments [6]. The internal body is enclosed within a 23 mm-diameter (OD) stainless steel closed-one-end tube, approximately 90 mm-long. A 4 mm-diameter orifice is drilled in the closed end of the tube. Such a cathode is sometimes called “orificed hollow cathode” in the literature. The internal body of the cathode and the external body are electrically insulated from each other with an insulator located between their flanges. Therefore the external body of the cathode is electrically floating during the cathode operation. Xenon (N48 grade, 99.998% purity) is introduced into the cathode via a feed tube attached to the side of the external body of the cathode (Fig. 3*b*). The nominal mass flow rate is 0.4 mg.s^{-1} of Xe.

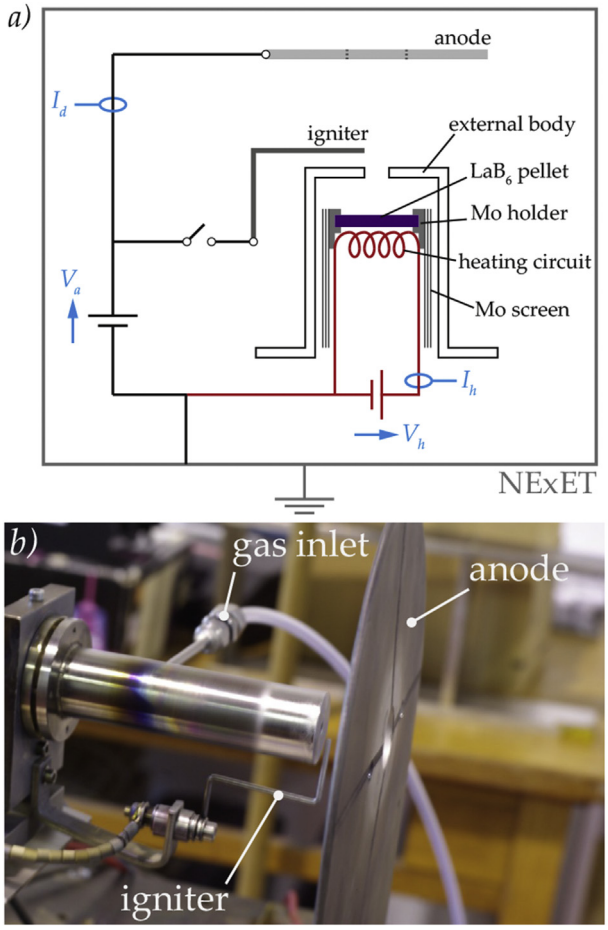

Fig. 3. Cathode in diode configuration: *a*) schematic of the electric setup, and *b*) picture of the cathode-anode setup.

The cathode is tested in diode configuration: it is placed in front of a stainless steel flat annular anode with a 210 mm outer diameter and a 21 mm inner diameter (Fig. 3*b*). The gap between the cathode body and the anode is 20 mm. The anode is positively biased with respect to the cathode body. Therefore the electrons extracted from the emitter surface are accelerated towards the anode. An external electrode, namely the igniter, is placed 3 mm downstream of the exit plane of the cathode orifice (Fig. 3*b*) and is used to ignite the cathode discharge by initiating the plasma breakdown. As soon as the discharge is ignited, the igniter is unpowered and allowed to float. No keeper electrode was required to operate the cathode within the current range studied in this work.

2.3. Instrumentation

2.3.1. Electrical measurements

The experiment was set up in a diode configuration. The heater was connected to a Midec power supply (SK 40-25, 40 V, 25 A). The anode was connected to an Elektro-Automatik power supply (EA-PSI 9200-70, 200 V, 70 A, 5 kW). The cathode base was grounded and the external body of the cathode was floating. Anode and heater voltages were measured using Tektronix voltage probes (P6139A, 500 MHz, 8.0 pF). The discharge current (*i.e.*, the anode current) was measured using a Tektronix current probe (TCP202, dc to 50 MHz bandwidth). Probes were connected to a Tektronix digital oscilloscope (TDS5104, 1 GHz, 5 GS.s^{-1}) to monitor and record the electrical signals at a sampling rate of 1 MHz.

2.3.2. Temperature measurements by thermocouples

Thermocouple measurements have proven to be challenging in LaB_6 cathodes because of the high temperatures of the electron-emitting insert and limited access to the cathode interior [9]. The very limited number of published papers shows the difficulty of measuring the emitting insert temperature during the cathode operation, although the LaB_6 insert temperature is one of the most important parameters to estimate its lifetime [6], which directly impacts the cathode lifetime. To the authors' knowledge, only one study from the Jet Propulsion Laboratory (U.S.A.) [9] presents a complete and detailed study of the direct measurement of the emitter temperature of a LaB_6 cathode used as electron source for HTs. For BaO-W inserts, more studies have been published on direct temperature measurements of the insert [30,31], since in this case the temperature is lower.

A type C (W5%Re/W26%Re) tungsten-rhenium thermocouple (Thermocoax) rated to 1800 °C was employed to measure the LaB_6 emitter temperature. A sheathed thermocouple was used to prevent degradation of the W-Re wires due to boron migration [9]. In order to ensure a good electrical insulation between the W-Re wires and the LaB_6 pellet, the hot junction of the thermocouple was insulated from the sheath. This thermocouple assembly consisted of a pair of W-Re wires in magnesia (MgO) insulation within a tantalum sheath 0.7 mm in diameter (OD). A tantalum sheath was preferred to a molybdenum one since it allows higher working temperatures [32]. The small sheath diameter allows this thermocouple to be flexible in return for a lower maximum working temperature (1800 °C versus 2300 °C for rigid sheath and greater-

diameter type C thermocouples). The type C thermocouple was routed into the cathode through a small hole in the external body and inserted in a small hole in the pellet holder. In addition, a small hole was made with diamond tools into the pellet (see the magnification in Fig. 4*b*), allowing the thermocouple to be in direct contact with the LaB_6 insert. To maintain this direct contact during the experiments, the type C thermocouple was mounted above the cathode in a downward direction and was fixed loosely to its support. The thermocouple was therefore lightly leaned on the insert lateral wall. Drilling of the external body of a cathode is a validated method to insert a thermocouple inside a cathode without modifying the cathode operation [33]. The type C thermocouple was further insulated by an alumina tube. This secondary layer of insulation was employed to avoid short circuits between the external body of the cathode (floating) and the LaB_6 pellet (grounded). Fig. 4 shows a detailed schematic of this particular thermocouple setup.

Additional thermocouples were used to monitor the temperature at several locations where temperatures were lower. Type N Nicrosil/Nisil thermocouples (Omega) rated to 1300 °C were therefore employed instead of type C thermocouples. Type N thermocouples were preferred to base-metal thermocouples (for instance, type K nickel-chromium/nickel-aluminum thermocouples) owing to the higher thermoelectric stability of the type N wire thermocouple, in particular at high temperatures. A Super OMEGACLAD ™ XL sheath was employed in order to minimize drift at high temperatures. Type N sheathed thermocouples secured with tungsten foils were employed to measure the temperature of the external body of the cathode, the cathode flange, the igniter, and the rear side of the anode (Fig. 4*b*). All the thermocouples are connected to PID temperature controllers (P.M.A, ECO 24) and signals were read and recorded by a computer at a sampling rate of 1 Hz.

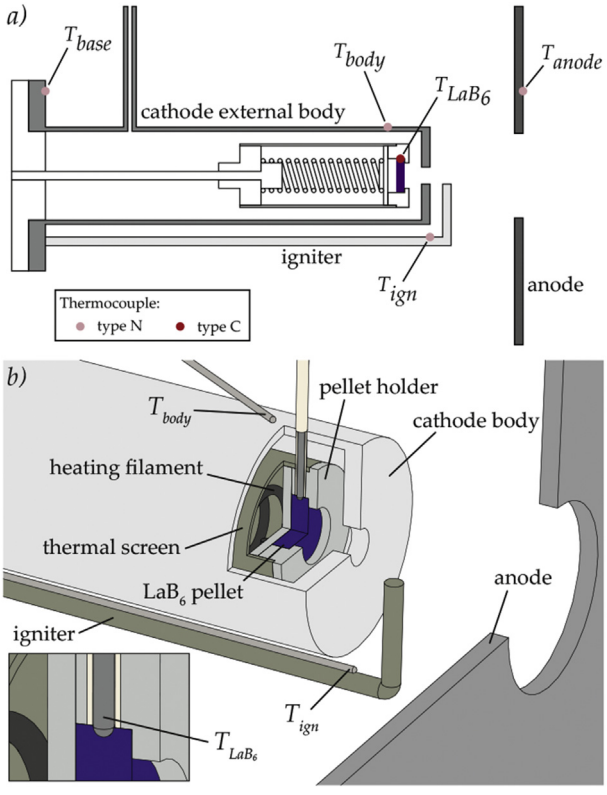

Fig. 4. Schematics of the thermocouple setup: *a*) thermocouple positions considered for the temperature measurements, and *b*) detailed view of the type C thermocouple setup.

2.4. Uncertainty analysis

The measurement uncertainties are estimated according to Abernethy *et al.* [34] and the error propagation law suggested by Kline and McClintock [35]. The total uncertainty ΔR of an experimental result R, which is a function of several variables $(\overline{X}_1, \overline{X}_2, \ldots, \overline{X}_J)$, takes into account the systematic uncertainties and the random uncertainties of the different variables. In this study, the systematic uncertainties include accuracy, sensitivity, stability, resolution, measurement error, linearization, cold-junction compensation; depending on the manufacturer data sheet of the measuring device (current/voltage probe, digital oscilloscope, thermocouple + controller). The random uncertainty corresponds to the standard deviation of the experimental measurements. The general expression of the total uncertainty ΔR calculated in considering a confidence interval of 95% is defined as follows [36]

$$\Delta R = \left[\sum_{i=1}^{J} \sum_{k=1}^{K} \left(\frac{\partial f}{\partial X_i} \Delta \overline{X}_i^k \right)^2 + \sum_{i=1}^{J} \left(t_{95} \frac{\partial f}{\partial X_i} X_{i,std} \right)^2 \right]^{1/2}, \qquad (1)$$

where $\Delta \overline{X}_i^k$ corresponds to the k-th type of systematic uncertainty of the i-th variable, t_{95} is the quantile of a two-tailed Student's t-distribution with a confidence interval of 95%, and $X_{i,std}$ is the standard deviation (unbiased estimator) of the i-th variable. In the case of a set of measurements where the measurement of R is repeated N times, t_{95} is divided by $N^{1/2}$ and the standard deviation of the N measurements is considered instead of $X_{i,std}$ [34]. The error-bars in 2D xy-plots represent the total uncertainty estimated with Eqn. (1). The plots were produced in Python, using the NumPy and Matplotlib environments [37,38].

3. Pre-ignition measurements

In this part, the cathode is studied without the plasma discharge. The heating current I_h is gradually increased from 2 A to 15 A with a 2 A-step, except for the last step (14 A–15 A). During each current step, the temperatures of the emitter T_{LaB_6}, the external body of the cathode T_{body}, the cathode base T_{base}, the igniter T_{ign}, and the anode T_{anode} are monitored. The duration of each step is set to 600 s which is long enough to ensure a steady-state temperature of the LaB_6 emitter at a given heating current. This duration was determined during long duration tests (30 min) at several heating currents. The steady-state temperatures for the pre-ignition measurements versus the heating current are shown in Fig. 5, where the error bars represent the total uncertainty calculated with Eqn. (1). For the electrical parameters of the heater, the following systematic uncertainties are considered: resolution (0.03%), accuracy read output (0.5% + 2 digit), and measurement error (2%). The total uncertainty of the temperature measurements takes into account the following uncertainties: resolution (0.2 °C), linearization (0.5 °C), cold-junction compensation (1.0 °C), controller error (0.1% + 1 digit), thermal stability (0.05%), impedance effect (0.5%), thermocouple error (1%), junction type effect (4%), contact effect (2%), radial gradient effect (−2% / +10%) for the emitter temperature, and the random uncertainty. The “radial gradient effect” is an asymmetric systematic uncertainty corresponding to the probable underestimation of the temperature pellet induced by a radial temperature gradient into the LaB_6 insert.

The emitter temperature (open squares, Fig. 5) is obviously the highest in comparison with the temperature of other parts, as expected since the LaB_6 pellet is the closest to the power source (*i.e.*,

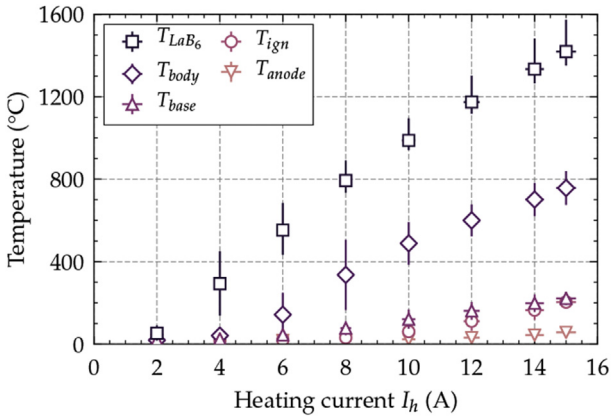

Fig. 5. Pre-ignition temperatures versus the heating current; no gas flow.

the heating filament). Fig. 6 shows a comparison between T_{LaB_6} and data from the literature [9]. Both temperature levels and trends are similar between the LaB_6 pellet (this study) and a cylindrical LaB_6 insert [9]. The main difference between these two data sets is an offset of about +200 °C. This discrepancy is due to the fact that the LaB_6 pellet is here in contact with the heating filament, which is not the case with a cylindrical insert [9], since an insulating material is placed between the insert and the heating element.

At $I_h = 15$ A (heating power of $P_h = 184.5$ W) the emitter temperature is about 1420 °C. This value of I_h corresponds to the one typically set to ignite our cathode [14]. In practice, the cathode ignition is allowed if the emitter temperature is higher than about 1300 °C. Similar temperature levels are reported in the literature: a pre-ignition temperature ranging between 1100 °C and 1400 °C allows the discharge to be ignited for a LaB_6 cathode with a cylindrical insert [8,9].

The temperature of the external body of the cathode T_{body} follows a more linear trend (Fig. 5). This element is heated by radiation from the heating circuit inside the cathode. The measured temperature of the external body is roughly half that of T_{LaB_6} (about 800 °C for $I_h = 15$ A), since a large gap of about 6 mm is set between the internal body of the cathode and the external one. The maximum temperature of the cathode base T_{base} is limited to about 200 °C. This suggests that heat losses through conduction in the external body of the cathode are weak. The rise of T_{ign} and T_{anode} is limited to a few tens of °C, since both the igniter and the anode are only heated by radiation of the cathode body during the pre-ignition phase. With this cathode design, the influence of the gas flow is negligible during the pre-ignition phase, since no significant temperature changes were observed with and without xenon flowing through the cathode.

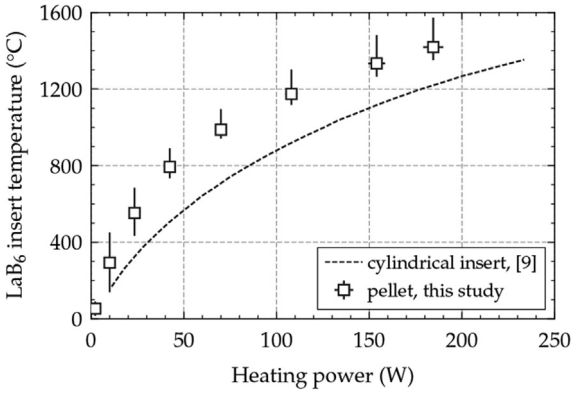

Fig. 6. Comparison of pre-ignition insert temperatures according to the heating power; no gas flow. The dotted line corresponds to experimental data from the literature [9].

4. Cathode operation

4.1. Operating envelope

Once the heating phase of the LaB_6 emitter has been achieved (*i.e.*, when $T_{LaB_6} > 1300$ °C), the discharge is ignited by applying a positive potential to the igniter. The ignition voltage typically ranges between 200 V and 300 V. The mass flow rate is set to 0.2 mg.s^{-1} of xenon and the discharge current is limited to 2 A. As soon as the plasma is present downstream of the cathode orifice, the ignition potential is applied to the anode and the igniter is allowed to float. Because the power supply of the discharge is used in a current-controlled configuration, the anode potential is free to vary and adapts to experimental configurations (*i.e.*, cathode design, mass flow rate, discharge current, etc.). During cathode operation, the heating power is maintained at about 185 W to ensure that the cathode does not switch off during experiments at low discharge current. The cathode can operate in self-heating mode at $I_d = 5$ A (*i.e.*, without external heating power), but insert heating by the bulk plasma is not sufficient to maintain the discharge at lower current values.

Fig. 7 shows the anode potential V_a versus the discharge current I_d, for three mass flow rates of xenon (0.2 mg.s^{-1}, 0.4 mg.s^{-1}, and 0.6 mg.s^{-1}). Each value of the two electrical parameters V_a and I_d is obtained by averaging three sets of two oscilloscope traces, each one lasting 200 ms. The record length of each time series is set to ensure a sufficiently high sampling frequency in order to provide an adequate cut-off frequency (500 kHz). After each increase in the current discharge, a waiting time of 600 s is applied before the first set of oscilloscope traces is recorded to ensure that the discharge is in steady state. The waiting time is obviously long, since the discharge physics is partially driven by heat transfer inside the cathode. Then, the second and third sets of oscilloscope traces are recorded after 1200 s and 1800 s, respectively. During each run, the value of the current discharge is kept unchanged. The total uncertainties of the discharge current/anode potential take into

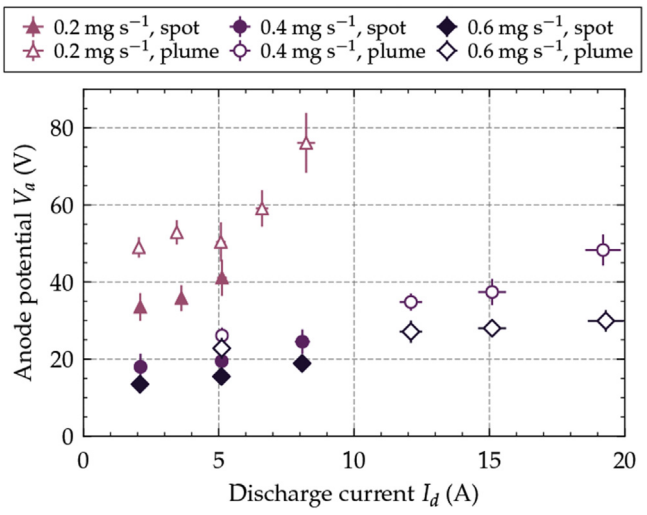

Fig. 7. Anode potential V_a according to the discharge current I_d for different mass flow rates of Xe. Closed and open symbols stand for spot mode and plume mode, respectively.

account the following sources of measurement uncertainty: power supply accuracy (0.2% / 0.1%) and regulation (0.2% / 0.07%), probe accuracy (3% / 0.5%) and sensitivity (40 mA / n/a), oscilloscope resolution (8 bits) and accuracy (1.5%).

Two discharge regimes are reported in Fig. 7: the spot mode and the plume mode. At a given mass flow rate, the working regime of the discharge changes when the current is progressively increased. For each mass flow rate tested in these experiments, there is a threshold value of I_d at which the plume mode is promoted. The occurrence of a spot-to-plume transition when the discharge current increases is not contradictory with the literature, though this behavior was not reported frequently in studies on HT cathodes operated in diode configuration. Several teams have indeed reported this behavior for different cathode designs and ranges of discharge current [39,40]. For our cathode design, a discharge current of 2 A is too high to observe the plume mode. This explains why spot mode was observed at the lowest values of I_d tested. Both working regimes of such a cathode in diode configuration are well known and described in the literature [26,27]. The physical meaning of these modes will be explained in the next section. The spot-to-plume transition is characterized by an increase in the average value of the anode voltage V_a of about 10 V, V_a being lower in the spot mode [41]. For a given value of I_d, it is possible to observe both regimes (not simultaneously) because there is a hysteresis [42]. Depending on how the discharge current is modified, positive ramp or negative ramp, the discharge can be operated in spot mode or in plume mode.

For this cathode design, the mass flow rate of 0.2 mg.s^{-1} is critical to run the cathode in spot mode, since the plume mode is easily promoted whatever the discharge current is. In addition, high and fast-growing values of V_a are measured when I_d is increased, which is the classical behavior of such a cathode [41,42]. In order to avoid very high values of V_a being reached, the discharge current is limited to 8 A when the mass flow rate is set to 0.2 mg.s^{-1} of Xe. Higher values of the Xe mass flow rate allow the discharge to be operated in spot mode if the discharge current is lower than 8 A. For a given discharge current, a minimum mass flow rate is indeed necessary to maintain the spot mode [43].

Both mass flow rates of 0.4 mg.s^{-1} and 0.6 mg.s^{-1} of Xe show similar trends: V_a rises when I_d increases and the plume mode is promoted if $I_d \geq 8$ A. The fact that similar trends are observed for different mass flow rates is expected with such a cathode setup, in particular when the cathode is operated in spot mode [43]. For these two mass flow rates (0.4 mg.s^{-1} and 0.6 mg.s^{-1}), the plume mode at $I_d = 5$ A is obtained with a negative current ramp. At a given discharge current one can observe that the higher the mass flow rate, the lower the anode potential, which is expected [43]. In these experiments, the mass flow rates of 0.4 mg.s^{-1} and 0.6 mg.s^{-1} of Xe are too low to ensure that the cathode will operate in spot mode if the discharge current is higher than 8 A.

4.2. Discharge modes

The classical discharge morphology of a cathode running either in spot mode or in plume mode is shown in Fig. 8. The spot mode is characterized by a small luminous spot observed just downstream of the cathode orifice [43]. This contrasts with the bright diverging plume that extends downstream of the cathode and beyond the anode in the case of plume mode. In addition to this bright plume, a dark space is sometimes observed a few millimeters downstream of the cathode orifice in the plume mode [44–46] (not visible in Fig. 8). This dark space is a region where the electron temperature is low, inducing a decrease in excitation of Xe atoms and therefore a faint luminosity [44]. Depending on the operating conditions, this dark space can be very close to the cathode orifice and consequently hardly visible to the naked eye.

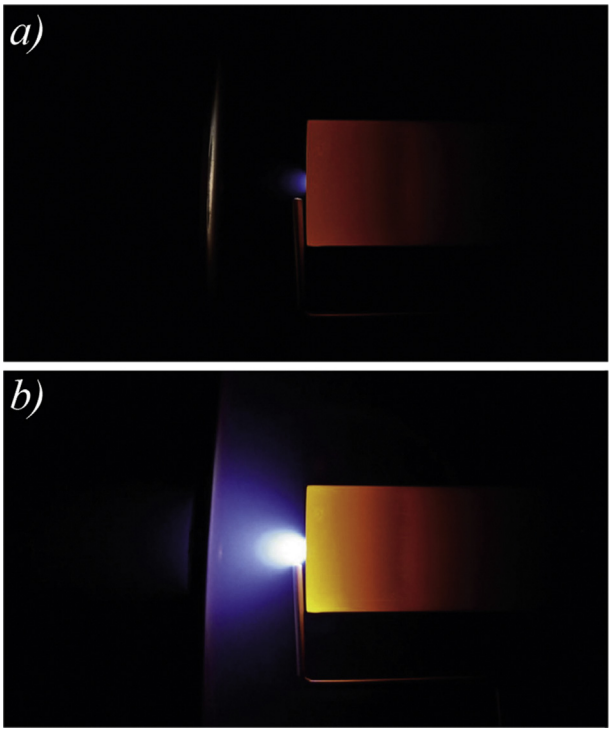

Fig. 8. Pictures of the plasma discharge operated in: *a)* spot mode at $I_d = 5$ A, and *b)* plume mode at $I_d = 12$ A. The mass flow rate is 0.4 mg.s^{-1} of Xe. The anode is on the left side. The exposure time is 50 ms.

Even though the visual morphology of the discharge can be used as a possible tool to determine what the discharge regime is, it is more relevant to study the standard deviation of the electrical parameters (I_d or V_a in this work) in order to determine the discharge mode beyond any doubt. Visual determination of the discharge regime can be tricky in some cases because other discharge modes with similar features to those of the plume mode can be observed [45]. The standard deviation of the discharge current $I_{d,std}$ is calculated using the classical unbiased estimator. The ratio of $I_{d,std}$ to I_d is estimated for each experimental case. Fig. 9 shows that a ratio $I_{d,std}/I_d$ below $\approx$10% is a good indicator of a discharge in spot mode, whatever the mass flow rate tested. In spot mode, fluctuations of the electrical parameters are very low, about 2% of the average value. This contrasts to the plume mode where the amplitude of the current fluctuations corresponds roughly to 10–30% of I_d.

The time traces plotted in Fig. 10 illustrate the different behaviors of the discharge current. As expected, the spot mode ($I_d = 5$ A) exhibits a very low level of fluctuations. By increasing the discharge current (at constant mass flow rate), the discharge regime changes into the plume mode (12 A and 19 A). One can see that a growing level of fluctuations appears in Fig. 10 when the discharge current is increased. The time traces in Fig. 10 are similar to the ones reported in the literature for HT cathodes [43,46]. The power spectral density of the current discharge is estimated from the time traces in order to determine the main frequencies of the current oscillations. Welch's method is used to plot the power spectra. This method is used because it reduces noise in comparison with the standard periodogram spectral estimating method.

Fig. 11 shows the power spectra of the time traces plotted in Fig. 10. The power spectrum corresponding to the spot mode ($I_d = 5$ A) is obviously less energetic [47], since a very low level of fluctuations was measured ($I_{d,std}/I_d \approx 2\%$). However, one can

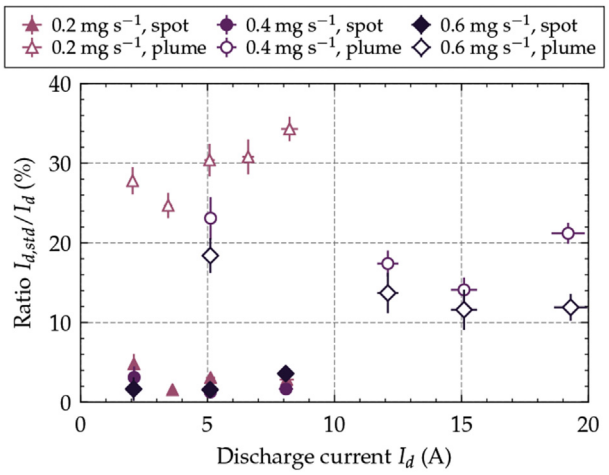

Fig. 9. Ratio of the standard deviation of I_d to the average value of I_d according to the discharge current for different mass flow rates of Xe. The closed and open symbols stand for spot mode and plume mode, respectively.

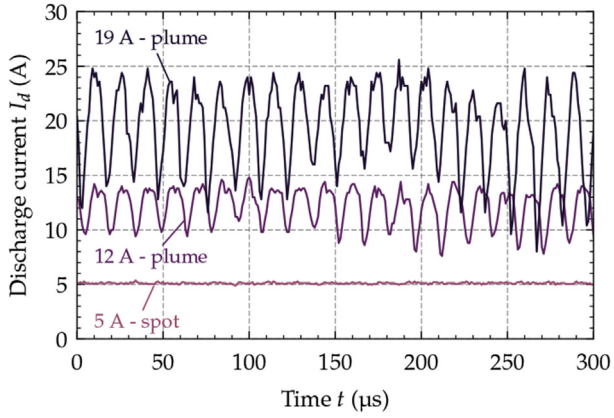

Fig. 10. Time series of the discharge current. The mass flow rate is 0.4 mg.s^{-1} of Xe.

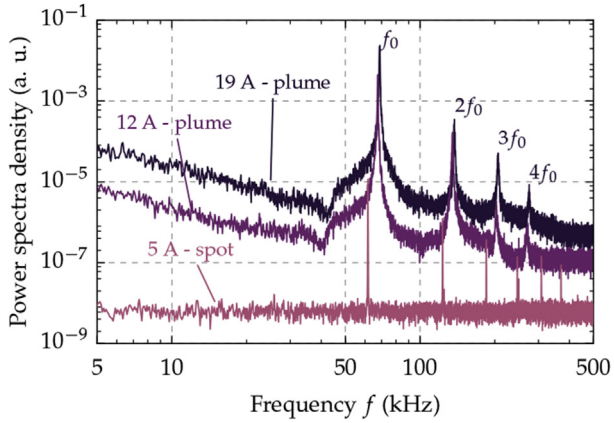

Fig. 11. Power spectral density of I_d according to the discharge current. The mass flow rate is 0.4 mg.s^{-1} of Xe.

observe a very narrow peak at $f_0 = 62.7$ kHz with its associated harmonics ($2f_0$, $3f_0$, etc.). The presence of these frequency peaks in a power spectrum corresponding to the spot mode indicates that the spot-to-plume transition is already promoted for this current value. This confirmed that the transition from spot mode to plume mode occurs continuously [46] as the discharge current increases or the mass flow rate decreases. If the discharge current is increased, the discharge mode will turn into plume mode. For every test case performed with the discharge in the spot mode, the overall aspect of the power spectrum is a low energy flat spectrum, with highly narrow peaks if the spot-to-plume transition occurs. For higher values of I_d, the discharge turns into plume mode and the power spectrum is greatly modified. The first dramatic change is due to the increased energy of the power spectra. The average energy level of each spectrum corresponding to the plume mode is a few orders of magnitude greater in comparison with the spot mode. The second modification is that the narrow peaks detected in spot mode are replaced by broader peaks clearly visible in the power spectra (both the fundamental and its harmonics).

Fig. 12 shows the fundamental frequency f_0 of the discharge current oscillations according to the discharge current. The data points correspond to the discharge operated in plume mode. It can be seen that the fundamental frequencies detected range between 50 kHz and 90 kHz. Our measurements of f_0 match the frequency range that is generally reported in the literature for plume-mode oscillations of HT cathodes operated in diode configuration [46,48,49]. Theses oscillations are related to ion-acoustic-like instabilities [50], including the electron/ion two-stream instability (also known as Buneman instability) and the ion acoustic instability. These instabilities typically occur when unmagnetized plasma carries current with the electrons drifting with respect to the ions [51]. It is therefore reasonable to associate the observed oscillations in plume mode with a current-driven instability. This type of instability is known to be responsible for nonclassical transport processes [51] and it was demonstrated that anomalous heating occurs in the orifice region [52] and the plume region (*i.e.*, downstream of the cathode) [53] of HT cathodes. The instability mode (Buneman or ion acoustic) depends on the plasma parameters [54]. In the case of HT cathodes operated in diode configuration, Mikellides *et al.* [53] show that different plasma regions (including the orifice and the plume regions) can be subject to the ion acoustic instability.

During operation of a cathode in diode configuration, three classes of discharge oscillations have been identified [46], each one corresponding to a particular type of physical phenomenon. The first class corresponds to high-frequency oscillations, in the 200 kHz-2 MHz range, which are associated to turbulent ion acoustic (IAT) oscillations. This type of oscillation has been recently confirmed experimentally [55] and is expected to occur

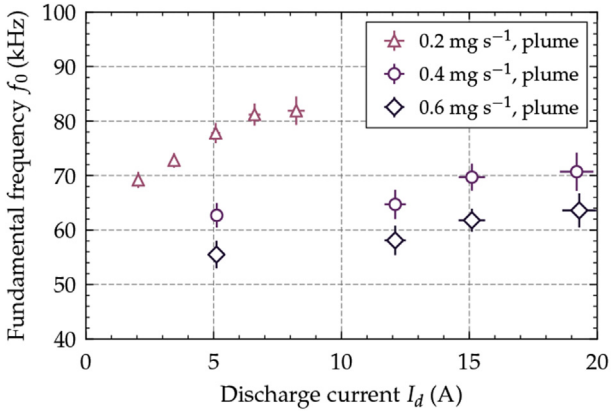

Fig. 12. Fundamental frequency f_0 according to the discharge current for different mass flow rates of Xe. The frequency f_0 is measured when the discharge is operated in plume mode.

predominantly for high current discharge [55] (>30–60 A), which is not the case of the present study. The second class corresponds to medium-frequency oscillations (40–200 kHz) that are associated with current-driven instabilities [46,49]. These oscillations can be related to two-stream (e-i) instability (Buneman instability) or ion-acoustic instability, depending on the plasma parameters [53]. Mikellides *et al.* [52,53] demonstrated that current-driven instabilities are responsible for the enhanced resistivity and nonclassical plasma transport in HT cathodes operated in diode configuration. The third class of oscillations identified in HT cathodes corresponds to low-frequency oscillations around 1 kHz induced by regulation of the discharge power supply. In the present study, such a type of oscillation was not clearly identified in the spectra.

One can observe that the fundamental frequency increases as the discharge current increases or the mass flow rate decreases. This is in agreement with experimental measurements reported in the literature by different research teams [45,46,49]. For a given cathode design, the modification of the oscillation frequency of current-driven instabilities with the discharge current and the mass flow rate is due to a modification of the plasma parameters [46,53]. Many different parameters have been proven to influence both the amplitude and the frequency of the fluctuations present when a cathode is operated in diode configuration [56]. With the present design, the orifice diameter (4 mm) is the main parameter explaining why the spot mode cannot be sustained at a moderate mass flow rate and a discharge current higher than 8 A. For instance, the NSTAR cathode (BaO-W cylindrical insert) is able to sustain a discharge current higher than 10 A with an orifice diameter of 1.0 mm [46,53].

5. Temperatures

Fig. 13 shows the steady-state temperatures measured with the thermocouples. Data for each mass flow rate are plotted versus the discharge current. At each current increment, the temperatures were allowed to reach steady state. In order to easily compare the different cases (0.2 mg.s^{-1}, 0.4 mg.s^{-1}, and 0.6 mg.s^{-1}), a temperature offset of a few °C (positive or negative) is applied to the cases with 0.2 mg.s^{-1} and 0.6 mg.s^{-1} of Xe, equalizing the temperatures at $I_d = 2$ A.

As expected, the higher the discharge current, the higher the temperature, whatever the measurement position. This phenomenon is explained by the higher energy that is transferred to the system when the current increases. In particular, the emitter temperature exhibits a clear increasing trend with the discharge current (Fig. 13*a*). This behavior is typical of HT cathodes and has been reported many times in the literature, including direct [9,30] and indirect [8,47,57] measurements with thermocouples of the emitter temperature during cathode operation. A direct measurement of the insert temperature using an optical pyrometer system shows the same trend [58]. Given the measurement positions considered in this study (Fig. 4), the highest temperature was measured for the LaB_6 pellet. Considering the design of the cathode, it is expected that the pellet holder temperature could be higher than the LaB_6 insert, since this holder was in direct contact with the emitter and surrounded by the plasma. However, the temperature of the pellet holder in contact with the bulk plasma cannot be measured in our cathode design.

As previously observed, the case with a mass flow rate of 0.2 mg.s^{-1} differs from the other two. The temperature trends with

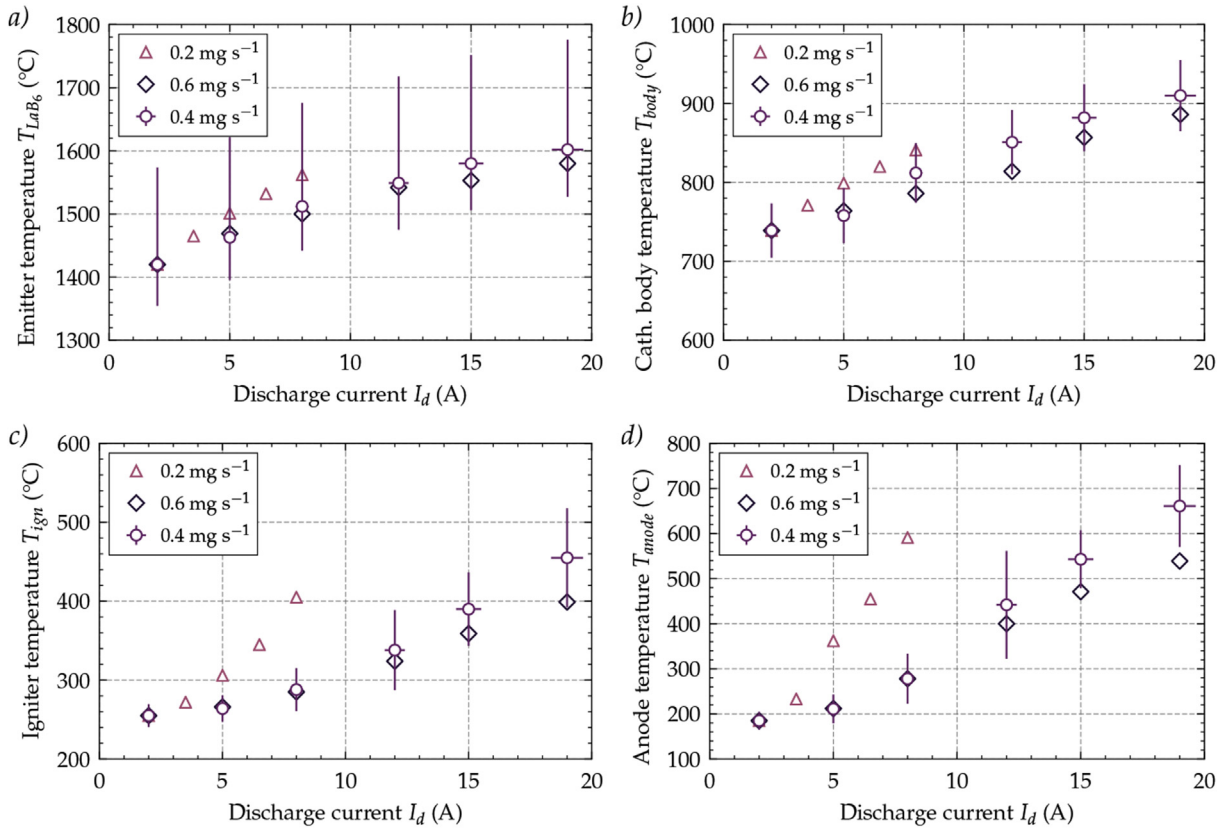

Fig. 13. Temperature measurements during cathode operation of: *a*) emitter temperature (T_{LaB_6}), *b*) external body of the cathode (T_{boby}), *c*) igniter temperature (T_{ign}), and *a*) anode temperature (T_{anode}). For clarity, only the error bars of the 4 mg.s^{-1}-case are shown.

the discharge current are similar but the slopes are much higher than those with 0.4 mg.s^{-1} and 0.6 mg.s^{-1}. The temperatures measured for this case are always the highest at a given value for the discharge current, including the temperature of the LaB_6 pellet. As concluded in the previous part, a mass flow rate of 0.2 mg.s^{-1} of Xe is the worst case tested to operate the cathode in decent conditions. In addition to the most energetic fluctuations, inducing a fast wear of the external body, the high insert temperature will indeed lead to a decreased lifetime of the cathode [57].

Whatever the measurement position considered, the onset of the plume mode does not induce a dramatic change in the temperature trend with the discharge current. This is relevant to the behavior reported in the literature for the orifice plate temperature [47]. One can observe that the temperatures of the emitter and other parts of the cathode decrease slightly with increasing mass flow rate (from 0.4 mg.s^{-1} to 0.6 mg.s^{-1}). The decrease in the insert temperature with the mass flow rate was reported for a BaO-W insert [58] and LaB_6 insert [9], for low-current operation (less than 20 A, typically). However, this trend is expected to reverse (*i.e.*, higher insert temperature for higher mass flow rates) for higher discharge current [9,30]. The same phenomenon is also expected to occur for the other parts of the cathode when the discharge current increases [57]. Even though the internal pressure is expected to be higher when the mass flow rate increases, a low mass flow rate means that the plume mode is present, in our cathode design. This results in an additional heating of the external body of the cathode due to the energetic ions returning onto this part of the cathode. In addition, the plume mode is also responsible for a higher heating of the anode due to the collection of electrons that are more energetic [43]. In return, supplementary heat fluxes are radiated from the anode and the inside face of the external body, both contributing to the overheating of the LaB_6 pellet measured when the mass flow rate is low. This assumption is supported by the fact that the temperature difference for the anode between 0.4 mg.s^{-1} and 0.6 mg.s^{-1} is higher than the one calculated for the LaB_6 pellet temperature.

Fig. 14 shows the emitter temperature for the mass flow rates of 0.4 mg.s^{-1} and 0.6 mg.s^{-1} of Xe and the temperature estimated from the Richardson-Dushman equation (thermionic emission) for different LaB_6 materials found in the literature, versus the current density j_{em} corresponding to the electron emission. Several work functions and values of the emission coefficients (*i.e.*, ϕ and A or D [7]) have been reported in the literature for LaB_6, depending on the measurement method of the emission coefficients, temperature range of the measurement, surface stoichiometry (La-to-B ratio), and crystal structure (single-crystal or polycrystalline emitter), to name a few factors. Table 1 shows the emission coefficients used to plot the estimated temperature in Fig. 14. It can be seen that Table 1 presents some references [6,59–61] suggested in the extensive work [7] of D.M. Goebel from the JPL. These references are frequently cited by many other teams in the context of LaB_6 HT cathodes. In addition, Table 1 also introduces three less-cited sets of emission coefficients [62–64].

The curves plotted in Fig. 14 correspond to the temperature calculated with the classical Richardson-Dushman equation $j_{em} = f(T, \phi)$ using the work function values of Table 1 and a current density based on an electron emission surface of 28.27 mm^2 (π(3mm)^2). The current density for the experimental data is estimated in considering that the electron current emitted at the pellet accounts for 75% of the total current. In HT cathodes, several sources contribute to the discharge current [65], including the thermionic electrons from the insert and the ions from the plasma. The ratio of the electron current emitted at the pellet to the total current depends on the cathode geometry [22], the insert material [66], and the operating conditions [24,66]. In the case of our

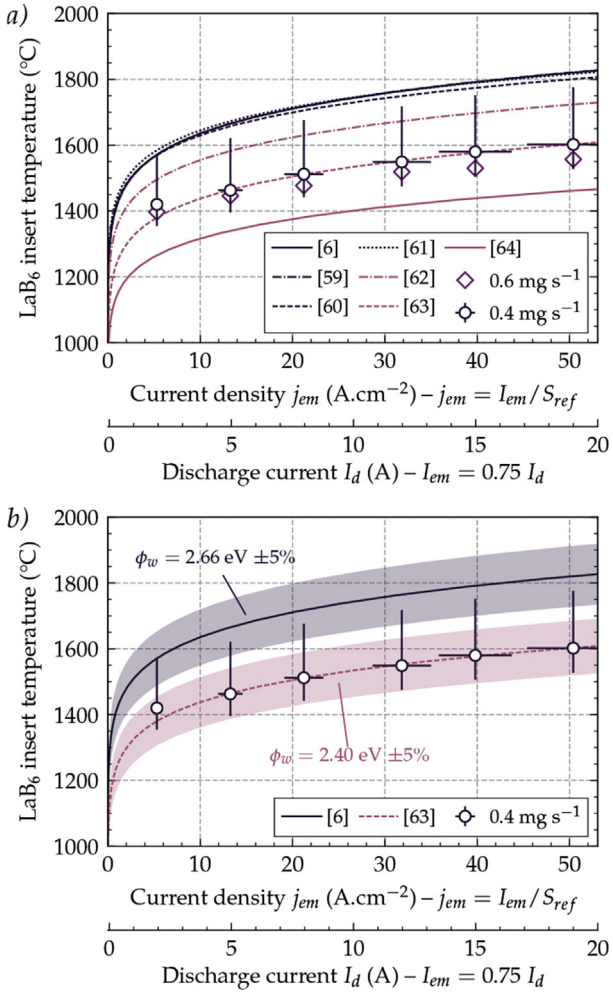

Fig. 14. Comparison of the experimental data (open symbols) of the LaB_6 insert temperature and the estimated temperature from the Richardson-Dushman equation: *a*) using the emission coefficients in Table 1, and *b*) modification of the estimated temperature for a variation of ±5% of the work function.

cathode design (LaB_6 insert, flat disk shape), this ratio is lower than 100% and ranges from 65% to 90% [23], depending on the operating conditions. The experimental points in Fig. 14 correspond to a current density j_{em} calculated with $I_{em} = 0.75 I_d$ and S_{ref}. The total uncertainty of the current density j_{em} is calculated with Eqn. (1) using the total uncertainties of the discharge current and the electron emission surface.

One can observe in Fig. 14*a* that experimental data (open symbols) are significantly lower than temperatures estimated with the Richardson-Dushman equation and the emission coefficients generally used in the studies dedicated to LaB_6 HT cathodes [7] (2.66 eV < ϕ < 2.91 eV, see Table 1). Such a difference between temperature measurements and emission curves have been reported recently for a high-current cathode with a cylindrical LaB_6 insert [9]. In our case, the discrepancy may be related to the temperature measurement of the LaB_6 insert, partly. An underestimation of the insert temperature due to the positioning of the thermocouple tip and/or a too high radial gradient within the insert can not be ruled out, definitely. To take into account this source of uncertainty, experimental points in Fig. 14 show quite large asymmetric error bars (−2% / +10%, see Sect. 3). Though the discrepancy is reduced in considering the measurement uncertainty, an other reason must be considered to explain the difference

Table 1
Work function ϕ and Richardson coefficient A (or D [7]) of sintered LaB_6.

From	ϕ (eV)	A ($A.cm^{-2}K^{-2}$)	Temp. range (°C)	Comment
Lafferty [6]	2.66	29	750–1000	
Kudintseva and Tsarev [62]	2.68	73	1500	
Kohl [59]	$2.66 + 1.23e^{-4}T$	120	750–1000	[6], T in K
Ahmed and Broers [63]	2.40	40	1450–1650	
Jacobson and Storms [60]	2.87	110	900–1150	$LaB_{6.01}$
Storms and Mueller [61]	2.91	120	1200–1400	
Pelletier and Pomot [64]	2.36	120	750–1050	38% porosity

between experimental data and the emission coefficients summarized in Goebel *et al.* [7].

As pointed out in a recent experimental study [9], the effective work function must be lower than the work function value taken from the literature to explain the discrepancies observed between experimental data and empirical curves. Plasma effects, such as Schottky effect and space charge effect, occur indeed during operation of HT cathodes [65] and can modify the effective value of the work function. If the plasma density is sufficiently high in the vicinity of the emitting insert, the effective work function is lower than the value taken from the literature due to the Schottky effect [25,52]. The Schottky-enhanced emission in HT cathodes is supported by a recent study [67]. Numerical simulations of a cathode with a BaO-W cylindrical insert have been performed and a work function reduction of about 0.1 eV ($\approx$5%) was reported by the authors [67]. In our cathode design, a reduction in work function of about 13–16% is required if one considers the emission coefficients generally used in the studies dedicated to the LaB_6 HT cathode [7] ($2.66\ eV < \phi < 2.91\ eV$). This is much higher than what plasma effects can induce (a few %) [23]. However, if a different set of emission coefficients [63] is considered, a more reasonable work function reduction, about 5%, is now required to match the temperature measurements in Fig. 14*a*. The uncertainty of the work function may also play a role in the discrepancy between experimental data and emission curves. Each value of ϕ was indeed determined experimentally and an uncertainty was estimated. As shown in Fig. 14*b*, the temperature estimated by the Richardson-Dushman equation depends a lot on the work function value. The colored bands in Fig. 14*b* correspond to a modification of $\pm$5% of ϕ.

The first conclusion of this comparison between experimental measurement of the insert temperature and estimated values (from the Richardson-Dushman equation) is that the insert temperature must be measured with a great care. This includes the listing of the relevant sources of uncertainties and their accurate quantification in the uncertainty budget. The second one is that the emission coefficients taken from the literature may not be sufficiently characteristic of the LaB_6 material used in the tested cathode. Our group has therefore just begun to develop a test bench to measure (by the Richardson plot method [60]) the emission coefficients of the same LaB_6 material as the one used in the cathode tested in the present study.

6. Conclusion

A laboratory model of a 5 A-class cathode (nominal condition: 5 A at 0.4 $mg.s^{-1}$ of Xe) has been experimentally studied in the diode configuration with a flat metal anode set instead of a HT. The cathode is used as electron source for gas ionization and plume neutralization in HTs. The cathode design studied here is based on the heating of a LaB_6 flat disk to emit electrons. The data gathered during the test campaign were used to investigate whether this design allows the cathode to be operated in spot mode. Three mass flow rates of Xe were tested (0.2 $mg.s^{-1}$, 0.4 $mg.s^{-1}$, and 0.6 $mg.s^{-1}$). Too high a mass flow rate of Xe is indeed not affordable. In view of future HT current requirements (*i.e.*, HT power), the 5 A-class cathode was operated with a discharge current ranging from 2 A to 19 A. Electrical parameters and temperature of several cathode parts, including the LaB_6 insert, were collected during the test campaign and analyzed.

The operating envelope that was experimentally determined shows that this cathode design is not optimized to operate in spot mode. The lowest mass flow rate of Xe tested (0.2 $mg.s^{-1}$) is critical, since the anode voltage is too high and the cathode operates in plume mode. For higher mass flow rates of Xe (0.4 $mg.s^{-1}$ and 0.6 $mg.s^{-1}$), the spot-to-plume transition was observed to occur as soon as the discharge current exceeds 8 A. This cathode design is therefore not adapted to high current applications. Strong fluctuations at well defined frequencies were detected using spectral analysis of I_d or V_a time series. These medium-frequency oscillations varying with the discharge current and the mass flow rate are related to ion-acoustic-like instabilities. These are known to be detrimental to vital cathode parts due to fast wear of the emitter and cathode body when occurring during cathode operation. In order to extend the operating envelope of this cathode design, we plan to reduce the orifice diameter, since this rather large size is suspected to be the main cause of plume mode onset. Concerning the development of a 100 A-class cathode, the present study confirm that a flat disk emitter is not a relevant design for high power applications. Such a shape will likely induce a too high current density ($> 15 - 20\ A.cm^{-2}$) that will be detrimental for the cathode lifetime. Numerical simulations of a 100 A-class cathode with a cylindrical insert have therefore been performed recently by our team in using the cathode code of LAPLACE (Toulouse, France) [25].

Temperature measurements performed with thermocouples reveal that the LaB_6 insert is reasonably heated during the cathode operation (about 1600 °C at 19 A), except for the lowest mass flow rate. The fact that temperatures decrease with increasing mass flow rate is consistent with the literature on LaB_6 cathodes operated a low discharge current (< 20 A, typically). Comparison between experimental results and temperatures estimated from the Richardson-Dushman equation using literature coefficients showed that measured temperatures seem too low in comparison with the emission coefficients widely used [6]. However, if a different set of emission coefficients [63] is used, the discrepancy between measurements and estimated temperatures is lower and can be explained by plasma effects occurring in such a cathode. In this case, the estimated temperatures match the measurements if the work function of LaB_6 decreases by 5%. In order to ascertain this, work is beginning in our group on the development of a test bench to measure the emission coefficient. The purpose is to characterize the same LaB_6 flat disk insert as the one used in the cathode tested in the present study.

Acknowledgments

This work is supported by the CNES Direction des Lanceurs Research and Technology Program. R. Joussot benefits from a CNES

post-doctoral fellowship and financial support from Safran. L. Grimaud benefits from a CNES-Région Centre Ph.D. Grant. The authors would furthermore like to acknowledge the constructive feedback from the reviewers.

References

[1] V. Kim, K.N. Kozubsky, V.M. Murashko, A.V. Semenkin, in: 30th International Electric Propulsion Conference, Florence, Italy, IEPC-2007-142, September 17-20, 2007, pp. 1–24.

[2] S. Mazouffre, Plasma Sources Sci. T 25 (2016) 033002, http://dx.doi.org/10.1088/0963-0252/25/3/033002.

[3] V. Kim, J. "Trudi MAI" (Moscow Aviat. Inst.) 60 (2012) 1–11.

[4] A.I. Morozov, Plasma Phys. Rep. 29 (2003) 235–250, http://dx.doi.org/10.1134/1.1561119.

[5] K.N. Kozubskii, V.M. Murashko, Y.P. Rylov, Y.V. Trifonov, V.P. Khodnenko, V. Kim, G.A. Popov, V.A. Obukhov, Plasma Phys. Rep. 29 (2003) 251–266, http://dx.doi.org/10.1134/1.1561120.

[6] J.M. Lafferty, J. Appl. Phys. 22 (1951) 299–309, http://dx.doi.org/10.1063/1.1699946.

[7] D.M. Goebel, R.M. Watkins, K.K. Jameson, J. Propul. Power 23 (2007) 552–558, http://dx.doi.org/10.2514/1.25475.

[8] M.L. Plasek, C.J. Wordingham, S. Roja Mata, E. Choueiri, J.E. Polk, in: 50th AIAA/ASME/SAE/ASEE Joint Propulsion Conference, Cleveland (OH), U.S.A, AIAA 2014-3825, July 28-30, 2014, pp. 1–14, http://dx.doi.org/10.2514/6.2014-3825.

[9] J.E. Polk, D.M. Goebel, P. Guerrero, in: Joint Conference of 30th International Symposium on Space Technology and Science, 34th International Electric Propulsion Conference and 6th Nano-satellite Symposium, Hyogo-Kobe, Japan, IEPC-2015-44/ISTS-2015-b-44, July 4-10, 2015, pp. 1–12.

[10] D. Pedrini, R. Albertoni, F. Paganucci, M. Andrenucci, J. Propul. Power 32 (2016) 1557–1561, http://dx.doi.org/10.2514/1.B35828.

[11] S. Mazouffre, A. Lejeune, in: 1st Space Access International Conference, Paris, France, September 21-23, 2011, pp. 1–10. Paper 2011-51.

[12] V.V. Zhurin, Industrial Ion Sources: Broadbeam Gridless Ion Source Technology, John Wiley & Sons, New York, 2012.

[13] S.D. Grishin, L.V. Leskov, Electric Rocket Thrusters of Space Apparatus, Mashinostroenie, Moscow, 1989 (in Russian).

[14] L. Albarède, Etudes expérimentales d'un propulseur à effet Hall - Comportement stationnaire et dynamique du flux d'électrons, Ph.D. thesis, Université d'Orléans, France, 2004.

[15] Z. Ning, D. Yu, H. Li, G. Yan, Plasma Sci. Technol. 11 (2009) 194–199, http://dx.doi.org/10.1088/1009-0630/11/2/12.

[16] J.D. Sommerville, L.B. King, J. Propul. Power 27 (2011) 744–753, http://dx.doi.org/10.2514/1.50123.

[17] L. Grimaud, A. Pétin, J. Vaudolon, S. Mazouffre, Rev. Sci. Instrum. 87 (2016) 043506, http://dx.doi.org/10.1063/1.4945563.

[18] J.M. Makela, L.B. King, D.R. Massey, E.C. Fossum, in: 41st AIAA/ASME/SAE/ASEE Joint Propulsion Conference & Exhibit, Tucson (AZ), U.S.A, AIAA 2005-4236, July 10-13, 2005, pp. 1–7, http://dx.doi.org/10.2514/6.2005-4236.

[19] J.M. Makela, D.R. Massey, L.B. King, J. Propul. Power 24 (2008) 142–146, http://dx.doi.org/10.2514/1.29389.

[20] R.L. Washeleski, L.B. King, in: 45th AIAA/ASME/SAE/ASEE Joint Propulsion Conference & Exhibit, Denver (CO), U.S.A, AIAA 2009-5199, August 2-5, 2009, pp. 1–21, http://dx.doi.org/10.2514/6.2009-5199.

[21] L. Albarède, V. Lago, P. Lasgorceix, M. Dudeck, A.I. Bugrova, K. Malik, in: 28th International Electric Propulsion Conference, Toulouse, France, IEPC-2003-333, March 17-21, 2003, pp. 1–18.

[22] G. Sary, Modélisation d'une cathode creuse pour propulseur à plasma, Ph.D. thesis, Université de Toulouse, Université Toulouse III-Paul Sabatier, France, 2016.

[23] G. Sary, R. Joussot, L. Grimaud, L. Garrigues, S. Mazouffre, B. Laurent, C. Boniface, S. Oriol, F. Masson, in: 35th International Electric Propulsion Conference, Atlanta (GA), U.S.A, IEPC-2017-486, October 8-12, 2017.

[24] I.G. Mikellides, I. Katz, D.M. Goebel, J.E. Polk, K.K. Jameson, Phys. Plasmas 13 (2006) 063504, http://dx.doi.org/10.1063/1.2208292.

[25] G. Sary, L. Garrigues, J.-P. Boeuf, Plasma Sources Sci. T 26 (2017) 055007, http://dx.doi.org/10.1088/1361-6595/aa6217.

[26] H.R. Kaufman, Technology of electron-bombardment ion thrusters, in: Advances in Electronics and Electron Physics, vol. 36, Academic Press, New-York, 1974, pp. 265–373.

[27] M.J. Mandell, I. Katz, in: 30th Joint Propulsion Conference and Exhibit, Indianapolis (IN), U.S.A, AIAA 94-3134, June 27-29, 1994, pp. 1–6, http://dx.doi.org/10.2514/6.1994-3134.

[28] V.K. Rawlin, E.V. Pawlik, J. Spacecr. Rockets 5 (1968) 814–820, http://dx.doi.org/10.2514/3.29363.

[29] M. Touzeau, M. Prioul, S. Roche, N. Gascon, C. Pérot, F. Darnon, S. Béchu, C. Philippe-Kadlec, L. Magne, P. Lasgorceix, D. Pagnon, A. Bouchoule, M. Dudeck, Plasma Phys. Contr. F. 42 (2000) B323, http://dx.doi.org/10.1088/0741-3335/42/12B/324.

[30] M. Coletti, S.B. Gabriel, in: 48th AIAA/ASME/SAE/ASEE Joint Propulsion Conference & Exhibit, Atlanta (GA), U.S.A, AIAA 2012-4081, 30 July-01 August, 2012, pp. 1–17, http://dx.doi.org/10.2514/6.2012-4081.

[31] Y. Ohkawa, T. Higuchi, Y. Hayakawa, K. Miyazaki, H. Nagano, in: 33rd International Electric Propulsion Conference, Washington D.C., U.S.A, IEPC-2013-364, October 6-10, 2013, pp. 1–9.

[32] Morice, R.; Lihrmann, M.; Favreau, J.-O.; Morel, E.; Megharfi, M.; in: 11e Congrès International de Métrologie, October 20-23, Toulon, France, pp. 1–5.

[33] K. Kubota, Y. Oshio, H. Watanabe, S. Cho, Y. Ohkawa, I. Funaki, in: 52nd AIAA/SAE/ASEE Joint Propulsion Conference, Salt Lake City (UT), U.S.A, AIAA 2016-4628, July 25-27, 2016, pp. 1–9, http://dx.doi.org/10.2514/6.2016-4628.

[34] R.B. Abernethy, R.P. Benedict, R.B. Dowdell, J. Fluid Eng.-T. ASME 107 (1985) 1614, http://dx.doi.org/10.1115/1.3242450.

[35] S.J. Kline, F.A. McClintock, Mech. Eng. 75 (1953) 3–8.

[36] R.P. Benedict, Fundamentals of Temperature, Pressure and Flow Measurements, John Wiley & Sons, New York, 1984.

[37] J.D. Hunter, Comput. Sci. Eng. 9 (2007) 90–95, http://dx.doi.org/10.1109/MCSE.2007.55.

[38] T.E. Oliphant, Comput. Sci. Eng. 9 (2007) 10–20, http://dx.doi.org/10.1109/MCSE.2007.58.

[39] D.M. Goebel, R.M. Watkins, in: 41st AIAA/ASME/SAE/ASEE Joint Propulsion Conference & Exhibit, Tucson (AZ), U.S.A, AIAA 2005-4239, July 10-13, 2005, pp. 1–9, http://dx.doi.org/10.2514/6.2005-4239.

[40] V. Vekselman, Y.E. Krasik, S. Gleizer, V.T. Gurovich, A. Warshavsky, L. Rabinovich, J. Propul. Power 29 (2013) 475–486, http://dx.doi.org/10.2514/1.B34628.

[41] D.E. Siegfried, P.J. Wilbur, in: 13th International Electric Propulsion Conference, San Diego (CA), U.S.A, AIAA 1978-705, April 25-27, 1978, pp. 1–11, http://dx.doi.org/10.2514/6.1978-705.

[42] L. Rehn, H.R. Kaufman, in: 13th International Electric Propulsion Conference, San Diego (CA), U.S.A, AIAA 1978-707, April 25-27, 1978, pp. 1–8, http://dx.doi.org/10.2514/6.1978-707.

[43] M. Domonkos, A. Gallimore, G.W. Jr, M. Patterson, in: 35th Joint Propulsion Conference and Exhibit, Los Angeles (CA), U.S.A, AIAA 99-2575, June 20-24, 1999, pp. 1–25, http://dx.doi.org/10.2514/6.1999-2575.

[44] D.M. Goebel, K.K. Jameson, R.M. Watkins, I. Katz, I.G. Mikellides, J. Appl. Phys. 98 (2005) 113302, http://dx.doi.org/10.1063/1.2135417.

[45] S. Sakai, T. Katayama, J. Aoyagi, H. Takegahara, in: 30th International Electric Propulsion Conference, Florence, Italy, IEPC-2007-215, September 17-20, 2007, pp. 1–7.

[46] D.M. Goebel, K.K. Jameson, I. Katz, I.G. Mikellides, Phys. Plasmas 14 (2007) 103508, http://dx.doi.org/10.1063/1.2784460.

[47] M.T. Domonkos, M.J. Patterson, A.D. Gallimore, J. Propul. Power 19 (2003) 438–443, http://dx.doi.org/10.2514/2.6127.

[48] D.M. Goebel, K. Jameson, I. Katz, I.G. Mikellides, J. Polk, in: 29th International Electric Propulsion Conference, Princeton (NJ), U.S.A, IEPC-2005-266, 31 October-4 November, 2005, pp. 1–18.

[49] K. Nishiyama, Y. Shimizu, I. Funaki, H. Kuninaka, K. Toki, J. Propul. Power 23 (2007) 513–521, http://dx.doi.org/10.2514/1.19473.

[50] D.S. Lemons, S.P. Gary, J. Geophys. Res.-Space 83 (1978) 1625–1632, http://dx.doi.org/10.1029/JA083iA04p01625.

[51] J.J. Rasmussen, in: F. Cap (Ed.), Waves and Instabilities in Plasmas, Springer-Verlag, Wien, 1994, pp. 117–170.

[52] I.G. Mikellides, I. Katz, D.M. Goebel, J.E. Polk, J. Appl. Phys. 98 (2005) 113303, http://dx.doi.org/10.1063/1.2135409.

[53] I.G. Mikellides, I. Katz, D.M. Goebel, K.K. Jameson, J. Appl. Phys. 101 (2007) 063301, http://dx.doi.org/10.1063/1.2710763.

[54] D.B. Melrose, Instabilities in Space and Laboratory Plasmas, Cambridge University Press, Cambridge, 1986.

[55] B.A. Jorns, I.G. Mikellides, D.M. Goebel, Phys. Rev. E 90 (2014) 063106, http://dx.doi.org/10.1103/PhysRevE.90.063106.

[56] S. Patterson, A. Malik, D. Fearn, in: 35th Joint Propulsion Conference and Exhibit, Los Angeles (CA), U.S.A, AIAA 99-2577, June 20-24, 1999, pp. 1–14, http://dx.doi.org/10.2514/6.1999-2577.

[57] H. Kamhawi, J. Van Noord, 48th AIAA/ASME/SAE/ASEE Joint Propulsion Conference & Exhibit, Atlanta (GA), U.S.A, AIAA 2012-4080, 30 July-01 August, 2012, pp. 1–13, http://dx.doi.org/10.2514/6.2012-4080.

[58] J. Polk, C. Marrese, B. Thornber, L. Dang, L. Johnson, in: 40th AIAA/ASME/SAE/ASEE Joint Propulsion Conference and Exhibit, Fort Lauderdale (FL), U.S.A, AIAA 2004-4116, July 11-14, 2004, pp. 1–17, http://dx.doi.org/10.2514/6.2004-4116.

[59] W.H. Kohl, Handbook of Materials and Techniques for Vacuum Devices, Van Nostrand Reinhold, New York, 1967.

[60] D.L. Jacobson, E.K. Storms, IEEE T. Plasma Sci. 6 (1978) 191–199, http://dx.doi.org/10.1109/TPS.1978.4317109.

[61] E.K. Storms, B. Mueller, J. Phys. Chem.-US 82 (1978) 51–59, http://dx.doi.org/10.1021/j100490a014.

[62] G.A. Kudintseva, B.M. Tsarev, Radiotekhnika I Elektron. 3 (1958) 428–429.

[63] H. Ahmed, A.N. Broers, J. Appl. Phys. 43 (1972) 2185–2192, http://dx.doi.org/10.1063/1.1661472.

[64] J. Pelletier, C. Pomot, Appl. Phys. Lett. 34 (1979) 249–251, http://dx.doi.org/10.1063/1.90769.

[65] L. Cassady, E. Choueiri, in: 40th AIAA/ASME/SAE/ASEE Joint Propulsion Conference and Exhibit, Fort Lauderdale (FL), U.S.A, AIAA 2004-3431, July 11-14, 2004, pp. 1–10, http://dx.doi.org/10.2514/6.2004-3431.

[66] G. Sary, L. Garrigues, J.-P. Boeuf, in: Joint Conference of 30th International Symposium on Space Technology and Science, 34th International Electric Propulsion Conference and 6th Nano-satellite Symposium, Hyogo-Kobe, Japan, IEPC-2015-14/ISTS-2015-b-14, July 4-10, 2015, pp. 1–15.

[67] G. Sary, L. Garrigues, J.-P. Boeuf, Plasma Sources Sci. T 26 (2017) 055008, http://dx.doi.org/10.1088/1361-6595/aa6210.